



Mineral Nanoparticle Aggregation Alters Contaminant Transport under Flow

Lian Zhou, Laurent Lassabatère, N Tan Luong, J.-F. Boily, Khalil Hanna

► To cite this version:

Lian Zhou, Laurent Lassabatère, N Tan Luong, J.-F. Boily, Khalil Hanna. Mineral Nanoparticle Aggregation Alters Contaminant Transport under Flow. *Environmental Science and Technology*, 2023, 57, pp.2415–2422. 10.1021/acs.est.2c09358 . hal-03971820

HAL Id: hal-03971820

<https://hal.science/hal-03971820>

Submitted on 9 Feb 2023

HAL is a multi-disciplinary open access archive for the deposit and dissemination of scientific research documents, whether they are published or not. The documents may come from teaching and research institutions in France or abroad, or from public or private research centers.

L'archive ouverte pluridisciplinaire **HAL**, est destinée au dépôt et à la diffusion de documents scientifiques de niveau recherche, publiés ou non, émanant des établissements d'enseignement et de recherche français ou étrangers, des laboratoires publics ou privés.

Mineral nanoparticle aggregation alters contaminant transport under flow

Lian Zhou¹, Laurent Lassabatere², N. Tan Luong³, Jean-François Boily³, Khalil Hanna^{1*}

¹ Université Rennes, Ecole Nationale Supérieure de Chimie de Rennes, UMR CNRS 6226, 11

Allée de Beaulieu, F-35708 Rennes Cedex 7, France

² Université Lyon, Université Claude Bernard Lyon 1, CNRS, ENTPE, UMR5023 LEHNA Vaulx-en-

Velin, France

³Department of Chemistry, Umeå University, Umeå, SE-901 87, Sweden

*Corresponding author: Tel.: +33 2 23 23 80 27; khalil.hanna@ensc-rennes.fr

Abstract

Iron oxyhydroxide nanoparticle reactivity has been widely investigated, yet little is still known on how particle aggregation controls the mobility and transport of environmental compounds. Here, we examine how aggregates of goethite (α -FeOOH) nanoparticle deposited on 100-300 μ m quartz particles ($G_{ag}CS$), alter the transport of two emerging contaminants, and two naturally occurring inorganic ligands—silicates and phosphates. Bromide tracer experiments showed no water fractionation into mobile and immobile water zones in an individual goethite-coated sand (GCS) column, whereas around 10% of the total water was immobile in a $G_{ag}CS$ column. Reactive compounds were, in contrast, considerably more mobile and affected by diffusion-limited processes. A new simulation approach coupling the mobile-immobile equation with surface complexation reactions to surface reactive sites suggests that ~90% of the binding sites were likely within the intra-aggregate zones, and that the mass transfer between mobile and immobile fractions was the rate-limited step. This diffusion-controlled process also affected synergetic and competitive binding, which have otherwise been observed for organic and inorganic compounds at goethite surfaces. These results thereby call for more attention on transport studies, where tracer or conservative tests are often used to describe the reactive transport of environmentally relevant molecules.

Keywords: nano-aggregates; reactivity; diffusion; mass transfer; immobile water; simulation.

42

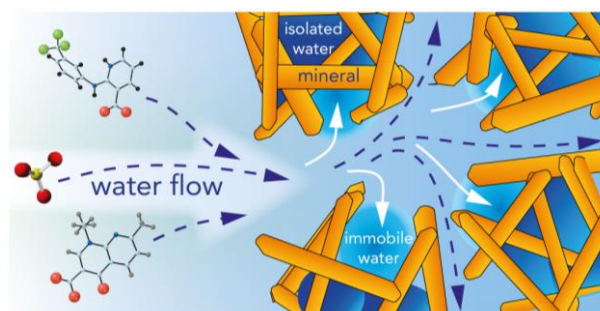
Synopsis

43 This work shows how diffusion-limited processes resulting from reactive nanoparticle
44 aggregation alter binding dynamics and reactive transport in porous media.

45

46

Graphical Abstract



1. INTRODUCTION

Pedogenesis commonly produces (micro- and macro-) aggregates of reactive mineral particles.¹⁻³ As these aggregates are responsible for multi-modal pore size distributions, with small pores inside the aggregates and large inter-aggregate pores⁴, they have a propensity to alter solute transport.⁵ The two-region two-porosity type model⁶ is commonly used to describe such systems, and requires the assumption of two types of water fractions in the pore space—mobile water (inside macropores or inter-aggregate pores) and immobile water (inside micropores or intra-aggregate pores). Advection-dominated transport in the mobile water is accompanied by diffusive mass transfer of solutes between the mobile and immobile fractions.^{7,8} In addition to physical processes, chemical interactions with environmental reactive surfaces, such as minerals, could also affect the mobility and fate of dissolved species.

Fe-oxyhydroxides are commonly found as minerals in environmental settings with different characteristics such as crystallinity, stability, specific surface area, and reactivity.⁹ These characteristics influence the biogeochemical cycling and availability of elements and the transport and mobility of organic and inorganic compounds. Goethite (α -FeOOH), the most abundant mineral of the iron oxide family, comes in a large variety of shapes and sizes.¹⁰ Goethite generally does not occur as homogeneous assemblages, and frequently forms coatings on less soluble and less reactive soil particles, such as silica sand.¹¹ Moreover, Fe-oxyhydroxides may occur in homo-aggregate and/or hetero-aggregate structures in subsurface environments.¹¹⁻¹⁴ As most reactive (sorption and redox) surfaces are controlled kinetically by reaction steps on

oxide surfaces, mineral aggregates likely have a significantly different reactivity from their individual oxide counterparts. However, much of our knowledge concerning contaminant-mineral interactions at the molecular level is derived from extensive experimentation on pure mineral phases.^{15–17} Although this literature provides a foundation for understanding reactive surface functional groups on individual mineral phases, chemical and physical phenomena in such homo-aggregated systems information cannot be readily extrapolated to those in complex hetero-aggregated mineral systems.

In this study, we examined how goethite aggregates obtained from freezing-thawing of fresh synthesized goethite particles¹⁸ affect the adsorption dynamics and transport of reactive solutes in column experiments. Silicate and phosphate were chosen as they are two major oxyanions in soil-water systems,¹⁹ and govern a wide range of biogeochemical processes such as contaminant fate and transport. Transport behaviors of nalidixic acid (NA), a quinolone antibiotic, and niflumic acid (NFA), an anti-inflammatory agent, were investigated because they are widely used in human and veterinary medicine, and are frequently detected in aquatic systems.^{20,21} A better understanding of the molecular-level mechanisms of previously investigated^{17,22–25} species binding to goethite surface sites could greatly improve our understanding of reactive transport behavior. Here, we focused on how the aggregates impact previously observed cooperative binding of NA/NFA, as well as competition adsorption of NA with dissolved phosphate (P) at goethite surfaces. Two kinds of coated sand were synthesized to mimic typical mineral coatings in environmental settings, goethite-

coated sand (GCS) and goethite aggregate-coated sand ($G_{ag}CS$). After characterizing the hydrodynamic regime using a non-reactive bromide tracer and stop flow method, breakthrough curves (BTCs) of reactive solutes were determined with different inflow conditions. The BTCs of reactive solutes were then described by coupling mobile-immobile model with surface complexation reactions onto goethite surfaces using PHREEQC-2.

2. MATERIALS AND METHODS

2.1. Materials. All reagents were purchased from Sigma-Aldrich and used without further purification. All solutions were prepared with ultrapure water and no contact with glass surfaces during preparation to prevent silica contamination (see Supporting Information (SI) for more details). Quartz sand from Fontainebleau (100–300 μm) was purchased from VWR Prolabo (France). The sand was washed with HCl and H_2O_2 and then with ultrapure water several times to remove impurities.

2.2 Synthesis of goethite and goethite aggregates. Goethite was synthesized as described in previous studies^{26–28} (see SI for more details). The purity of goethite was confirmed by X-ray diffraction (XRD). The Brunauer, Emmett, and Teller (BET) specific surface area of the synthetic goethite was 91 ± 1 m^2/g , determined by multipoint adsorption isotherm of N_2 (g) onto goethite. The point of zero charge (PZC) of goethite, determined at 298 K in 0.01, 0.1, and 1 M NaCl solutions by the potentiometric titration

method, was 9.1. Our previous TEM investigations showed that goethite particles were acicular in shape, with lengths in the 200-400 nm and widths in the 10-20 nm range.

Goethite aggregates were synthesized using a previously established freezing-thawing method¹⁸, as described in the SI. XRD and BET data showed that freezing-thawing and drying did not affect the crystal structure or the specific surface area of goethite. The size distribution of pores (Figure S1) in goethite aggregates was evaluated by applying the Barrett–Joyner–Halenda (BJH) method (assuming cylindrical pore shape) to the N₂ gas desorption isotherm data.

Water vapor adsorption and desorption measurements were conducted to check the effects of aggregation on the distribution of hydroxo-groups of the goethite surface. The results (Figure S2) confirmed no modification of the distribution of hydroxo groups between unaggregated and aggregated goethite. More information about characterization is given in the SI. Details about the synthesis of individual goethite-coated sand (GCS) and aggregated goethite-coated sand (G_{ag}CS) are also reported in the SI. According to iron measurements, the goethite content in GCS and G_{ag}CS was 1 ± 0.02 wt%.

2.3. Column experiments. Continuous flow-through experiments were conducted at room temperature and under water-saturated conditions. Columns (1.6 cm internal diameter) were packed with 15 g of GCS or G_{ag}CS, which provided the same bed length (4.9 ± 0.1 cm) and the same bulk density (1.55 ± 0.05 g/cm³). The columns were wetted upward with a 0.01 M NaCl background electrolyte solution at a flow rate of 0.5 mL/min (Darcian velocity of 14.92 cm/h) for 24 h to reach water-saturated conditions.

Pore volume (PV) for GCS and G_{ag}CS columns was determined by weighing and was 4.3 ± 0.1 mL and 4.1 ± 0.1 mL, respectively. Once the columns were saturated, flow characteristics of the porous bed were determined by injecting a 2-mL pulse of tracer solution (0.05 M NaBr) followed by 10 PV of 0.01 M NaCl at a flow rate of 0.5 mL/min. Solutions of 0.05 M NaBr were prepared with 0.01-M NaCl background electrolyte. In addition, two independent sets of flow-interruption experiments with step-injection of tracer solution (0.05 M NaBr) were performed for GCS and G_{ag}CS columns. The duration of flow-interruption was set to 12 hours. For all tracer experiments, the tracer experimental BTC in each experiment was determined by continuously measuring effluent conductivity.

After tracer experiments, reactive transport experiments were first conducted with a step injection of 10-μM NA solution (0.01-M NaCl and at pH 5) into GCS and G_{ag}CS columns at constant flow rate of 0.5 mL/min. In addition to the organic ligand, two sets of column experiments were performed for dissolved silicate (Si), which followed the step-injection of two concentrations of Si solutions (1000- and 2000-μM Si in 0.01 M NaCl at pH 5) into GCS and G_{ag}CS columns at the same flow rate. Furthermore, synergistic adsorption of NA/NFA and competitive adsorption of NA/P on goethite were investigated by injecting 10-μM NA with 10-μM NFA or 10-μM NA with 100-μM P into both columns at a constant flow rate of 0.5 mL/min. The background electrolyte concentration of the injected solution was 0.01-M NaCl at pH 5. Continuous on-line pH measurements were performed using pre-calibrated pH flow through a sensor in all breakthrough experiments. In addition, the pH of collected fractions was

160 routinely checked using a pH meter. Each column experiment has been duplicated
161 (regardless of injection with single or multiple compounds), i.e. two new packed
162 columns within two independent sets of flow-through experiments. In addition, tracer
163 experiments have been conducted for each new column. As such, the discrepancy in
164 G_{agCS} vs GCS was systematically confirmed through different columns tests in several
165 independent sets and using various kinds of solutes.

166 Soluble Si and P were determined by molybdenum blue spectrophotometric
167 methods.²⁹ The measurement error of this method was no more than 3%.
168 Concentrations of NA and NFA in the collected fractions were determined by a high-
169 performance liquid chromatography (HPLC) system equipped with an auto sampler
170 (Waters 717 plus) using a C18 column (250 mm×4.6 mm i.d., 5 μ m) and a UV detector.
171 The mobile phase was a mixture of water/acetonitrile (60:40 v/v) containing 0.1% of
172 formic acid. The flow rate of the mobile phase was set at 1 mL/min in isocratic mode
173 for the HPLC analysis. The UV detector was set to 258 nm for NA and 283 nm for
174 NFA. The estimated error for NA and NFA was 5%. Solute elution was characterized
175 by the BTC, namely through relative concentration (C/C_0) vs. injected PV. All column
176 experiments were terminated when the effluent concentration reached a steady-state
177 value.

178 **2.4. Surface complexation modeling.** Surface complexation modeling was done with
179 geochemical speciation code PHREEQC-2.³⁰ The charge-distribution multisite
180 complexation (CD-MUSIC) model³¹ was used to calculate surface species of two
181 organic ligands (NA and NFA) and two oxyanions (Si and P) on goethite. More details

are reported in the SI, and the surface complexation reactions of all surface species as well as the protonation constants of surface groups are reported in Table S1.

2.5. Surface complexation modeling combined with kinetics. Prevailing non-equilibrium conditions required implementation of kinetics in surface complexation reactions. NA can form metal-bonded (MB), (hydrogen-bonded) HB, and outer-sphere (OS) complexes,¹⁷ a result confirmed by our ATR-FTIR data (Figure S3). To describe adsorption kinetics of Si and P on goethite, we propose a multiple-site equilibrium/kinetic surface reaction expression, which was modified from a two-site equilibrium/kinetic sorption model³² and a multi-rate surface reaction expression.³³ All details about the modeling approach are reported in the SI.

2.6. Reactive transport modeling. To model reactive solute transfer under dynamic conditions, we coupled the transport module with surface complexation model considering both equilibrium and non-equilibrium reactions in PHREEQC-2. The transport module allows the simulation of advection and dispersion in relation with either advection-dispersion equation (ADE) or mobile-immobile model (MIM) approaches. More details including used equations, transport parameters and sensitivity analysis are reported in the SI.

3. RESULTS AND DISCUSSION

First, analysis of bromide BTCs with the moment method was performed as described in previous studies^{34,35} (see SI for more details). In both GCS and $G_{ag}CS$ columns, mass balance ratios estimated by the zero-order moment were close to unity, and retardation factors estimated by the first-order moment were slightly below 100%. These results revealed the presence of completely isolated water in both types of columns. Modeling with ADE for nonreactive tracer (equation S2.3) accurately reproduced bromide BTCs in GCS columns, and provided all the hydrodynamic parameters (isolated water fraction and dispersivity) needed for modeling. These parameters suggested that 15.3% of the total water volume was completely isolated, and that the immobile water fraction can be ignored. Flow in the $G_{ag}CS$ columns was, in contrast to GCS columns, heterogeneous because of water fractionation. MIM fitting (equations S2.4a-S2.4c, Figure S4 and Table S2), showed that 76.0% of the total water was free flowing, while the rest was either immobile (9.8%) or completely isolated (14.2%). The determined mass transfer rate constant ω is $1.48 \times 10^{-3} \text{ min}^{-1}$ (0.089 h^{-1}), and this falls within in the typical range ($\sim 0.03\text{--}0.09 \text{ h}^{-1}$)^{33,36} at similar scales and under similar injection conditions. The determined hydrodynamic parameters in both GCS and $G_{ag}CS$ columns were further validated by independent tracer experiments (Figure S5) conducted using flow-interruption method.

From these hydrodynamic parameters (Table S2), we could also estimate the characteristic times relative to advective and dispersive solute transport between the

mobile and immobile water. We find that exchange between these two water fractions was not instantaneous insofar as the mass transfer time ($T_{\omega} = 31.4$ min) was longer than the advection time ($T_{adv} = 6.2$ min). Using these hydrodynamic parameters (Table S2), we explored the mobility in non-aggregated and aggregated goethite-bearing columns of single compounds (Section 3.1) and of mixed compounds (Section 3.2).

3.1. Mobility of single compounds in GCS and G_{ag}CS columns

The experimental BTCs for NA obtained from GCS and G_{ag}CS columns had asymmetrical shapes (Figure 1), suggesting significant influence of rate-limited sorption process. The long tails observed in the BTC for NA in the GCS column was likely caused by chemical kinetic limitations. This was supported further by the mitigated tail of the NA BTC, obtained at a lower flow rate (0.1 mL/min) (Figure S6). Accordingly, our previous spectroscopic work¹⁷ showed that NA binds to reactive $\equiv\text{FeOH}^{-0.5}$ sites via hydrogen bonding and metal–carboxylate interactions, and MB formation is generally considered the rate-determining step.³⁷ In the G_{ag}CS column, the BTC for NA exhibited an early breakthrough (starting at around 3 PV), and had an extremely extended tail.

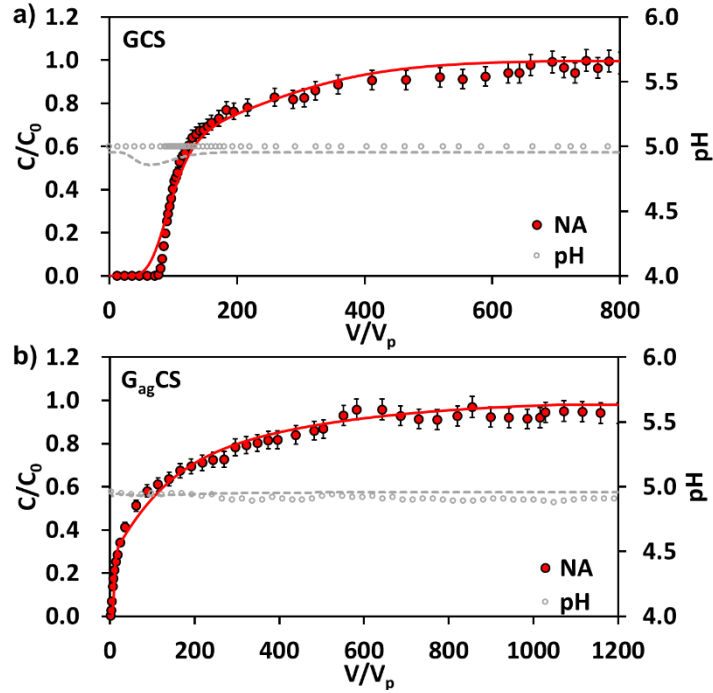


Figure 1. Experimental and modeled BTCs for NA and pH in GCS and $G_{ag}CS$ columns. Influent solutions of 10- μ M NA were injected in step-type concentration boundary condition. Inflow conditions: flow rate 0.5 mL/min, 10-mM NaCl background electrolyte inflow pH 5.0 ± 0.1 . Pore volumes of GCS columns and $G_{ag}CS$ columns are 4.3 ± 0.1 mL and 4.1 ± 0.1 mL, respectively. The solid and dashed lines are modeled BTCs for NA and pH obtained using PHREEQC-2, respectively.

The points correspond to the experimental data.

Due to the presence of immobile water fraction, this mobility behavior could be attributed to both chemical and physical non-equilibria through distribution of reactive sites in the intra-aggregate zones. Despite the observed discrepancy in breakthrough behavior in the GCS and $G_{ag}CS$ columns, NA surface loadings (estimated by zeroth moment analysis of the experimental BTC) was 0.28 NA/nm² in both columns when experiments were terminated. For GCS, the BTC for NA was well described by combining the classical ADE and two-step kinetic expression of surface complexation

reactions of NA onto goethite³⁸ (Figure 1). The macroscopic forward and backward kinetic rate constants in the column were 0.050 h^{-1} and 0.009 h^{-1} , respectively.

To account for the physical non-equilibrium in $G_{ag}CS$ column, the MIM transport module was coupled to the same two-step kinetic expression to simulate the NA transport behavior in $G_{ag}CS$ column. This approach was based on four hypotheses: i) NA adsorption in the mobile domain was mainly controlled by rate-determining chemical kinetics; ii) NA adsorption in the immobile domain was kinetically governed by diffusion at the interface between the mobile and immobile water fraction, diffusion into the immobile water fraction, and chemically rate-limited adsorption; iii) diffusion at the interface between the mobile and immobile water fractions and diffusion into the immobile water fraction was one integrated process and can be described with a constant first-order mass transfer coefficient $\omega \text{ (T}^{-1}\text{)}$; and iv) chemical kinetics for NA adsorption followed the same kinetic laws regardless of the location (at the surface of aggregates or inside the aggregates).

In the constructed model, the mass transfer coefficient $\omega \text{ (T}^{-1}\text{)}$ and fraction $f \text{ (}\%)$ were the only two optimizable parameters by fitting the experimental data. The other hydrodynamic parameters (mobile water content, the water content visited by the solutes, and the hydrodynamic dispersion coefficient) were fixed at the same values for all solutes, and derived from fitting the tracer BTCs. To investigate how these two parameters affected the shape of BTCs for NA, sensitivity analyses of parameter ω and f were performed (see SI for more details). Based on the results from sensitivity analyses (Figure S7), we found that parameters ω and f could be independently

determined by curve-fitting: f mainly governed the position of initial breakthrough point, whereas ω determined the turning point of relative concentration where the tailing starts. This ensures confidence for their estimates and proves that there is no concern about equifinality and non-uniqueness.

The best fit of the experimental BTC for NA in $G_{ag}CS$ column was obtained (Figure 1) when we considered the distribution of the sorption sites between mobile and immobile fraction, with around 10% sorption sites in contact with the mobile ($f = 10\%$) water fraction and the rest (90%) in contact with the immobile water fraction. The mass transfer coefficient ($\omega = 4.32 \text{ h}^{-1}$) relates to the diffusion from the mobile to the immobile water fractions and diffusion from the immobile water to sorption sites.

In conclusion, the transport behavior of NA through the aggregated $G_{ag}CS$ system was governed by a combination of two different processes. Adsorption first proceeded onto the most accessible surface sites, followed by adsorption to sites located within aggregates, and thus coupled to physical (*e.g.* diffusion within the intra-aggregate zones) and chemical non-equilibrium processes. Similar experimental phenomena were also reported in a previous study³⁹ where coupled mass transport and reactions in both intragranular and inter-granular domains described the spatial and temporal dependence of uranyl surface complexation rates in sediments.

To further validate the influence of aggregated systems on reactive solute transport and the distribution of reactive sites of goethite in $G_{ag}CS$ columns, we performed column experiments for silicate solutions in both GCS and $G_{ag}CS$ columns under similar flow-through conditions. Like NA, BTC for Si exhibited discrepancy between

the two types of columns (Figure 2). The shape of the experimental BTC for silicate was more asymmetrical in the $G_{ag}CS$ column as it has an earlier breakthrough point and extended tailing (Figure 2b). This essentially points to physical limitations within aggregated porous media. In GCS columns, silicate surface loadings, estimated by integrating the area above the BTC, were $\sim 0.58 \text{ Si/nm}^2$ at 1 mM and $\sim 0.78 \text{ Si/nm}^2$ at 2 mM. Only a slight increase of silicate surface loadings was found in $G_{ag}CS$ column, reaching $\sim 0.62 \text{ Si/nm}^2$ at 1 mM and $\sim 0.85 \text{ Si/nm}^2$ at 2 mM. As oligomerization and polymerization reactions only occurred when monomer silicates attach to existing MB Si species at high Si surface loading ($\sim 1 \text{ Si/nm}^2$),²⁵ no oligomerization and polymerization reactions were expected in these two columns.

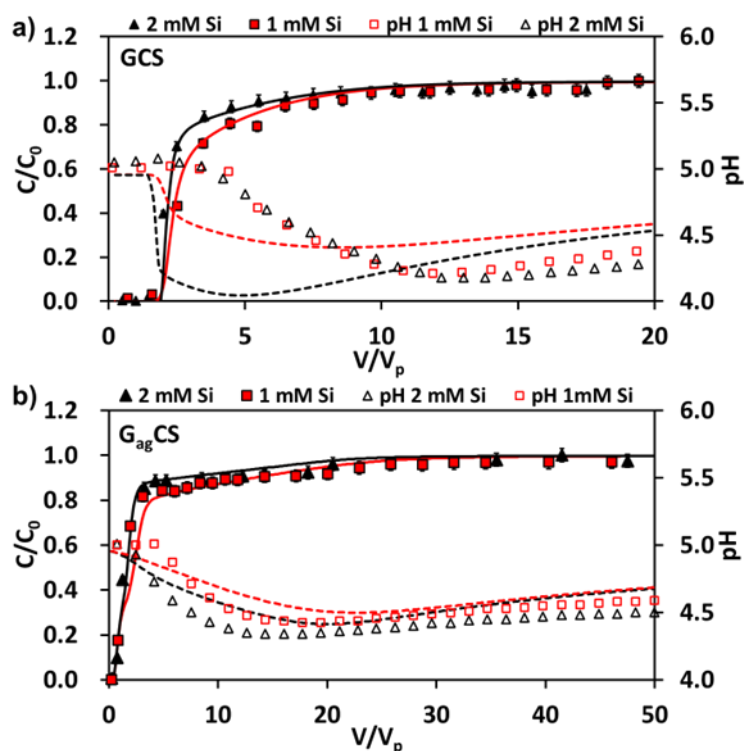


Figure 2. Experimental and modeled BTCs for Si and pH in GCS (a) and $G_{ag}CS$ columns (b). Influent solutions of 1-mM and 2-mM Si were injected in step-type concentration boundary condition. Inflow

conditions: flow rate 0.5 mL/min, 10-mM NaCl background electrolyte inflow pH 5.0 ± 0.1 . Pore volumes of GCS columns and $G_{ag}CS$ columns are 4.3 ± 0.1 mL and 4.1 ± 0.1 mL, respectively. The solid and dashed lines are modeled BTCs for Si and pH, respectively. The points correspond to the experimental data.

Incorporating the concept of two-site equilibrium/kinetic sorption³² into the multi-rate surface reaction expression, the BTCs for Si in GCS columns were well described by combining surface complexation parameters with only Si monodentate species (Si surface loadings below ~ 1 Si/nm²) and ADE transport parameters. In this model setup, the ratio between equilibrium sorption sites and kinetic sorption sites was set to equal 1:1 (Table S3), a ratio also used in a previous study.³⁸ Because this semi-empirical model describes a chemical nonequilibrium, pH variation was not well captured (Figure 2a).

To simulate the BTCs for silicate in $G_{ag}CS$ columns, multi-site equilibrium/kinetic sorption was merged into the multi-rate surface reaction expression to consider the distribution of sorption sites in the mobile/immobile water fractions. Coupling SCM, including surface reactions of silicate monodentate species with MIM transport model (same transport parameters for NA were used, including $f = 10\%$ and $\omega = 4.32$ h⁻¹), adequately reproduced the breakthrough behaviors of Si at two influent concentrations (Figure 2b). The need to couple multi-site equilibrium/kinetic sorption with MIM model suggests a combined chemical and physical non-equilibria. The quality of fitting between the modeled and experimental BTCs for pH was also improved in comparison to the case of GCS columns (Figures 2b vs. 2a, pH). The best fitting and related

optimized parameters (Table S3) suggest that all sorption sites located in the mobile domain are kinetically-limited. Moreover, the ratio between equilibrium and kinetic sorption sites located in the immobile domain was 1:9.

Model validation confirmed around 10% sorption sites were in contact with the mobile water fraction at the column scale, leaving the rest (90%) in contact with the immobile water fraction. Moreover, the mass transfer coefficients of reactive solutes (NA or silicate) were 2 orders of magnitude higher than nonreactive solute Br^- . This disparity may be explained by the difference in concentration gradient within the internal pores and the coupling between physical (flow field) and chemical (solute ionic radius, molecular diffusion, etc.) processes. Similar results have been reported in a previous study,⁴⁰ which showed that diffusion-controlled adsorption rate of arsenate onto porous ferric hydroxide depends on particle size.

Since the coupled processes of physical and chemical nonequilibria appeared to control the breakthrough behavior of reactive solutes in $G_{\text{ag}}\text{CS}$ columns, we checked whether a simplified model could be developed to simulate the breakthrough behaviors using an overall rate of both of the processes. This approach required that assumption that the combined processes of physical non-equilibrium and chemical kinetics occurring within the internal pores of aggregates (immobile domain) follow a first-order kinetic law, and can be described by a single mass transfer coefficient as required in MIM. In other words, physical and chemical non-equilibria are lumped into physical non-equilibrium, an “implicit” approach with respect to the “explicit” one previously mentioned.

We applied this implicit approach to model the reactive transport of silicate and NA in G_{ag}CS columns. Considering the fast adsorption onto most accessible surface sites located in the mobile domain, this process can be considered instantaneous and can be described using an equilibrium-based SCM. The modeling results (Figures S8 and S9a) showed that the breakthrough behavior of silicate can be captured using this approach provided that the mass transfer coefficient ω is optimized and set to 0.05 h⁻¹. However, this approach did not fit well with the time evolution of pH. We named this coefficient ω_{overall} since the optimized value of ω can be considered an overall mass transfer coefficient, which may be affected by various chemical and physical factors in the immobile water fraction. Our parameter ω_{overall} was used not only for silicate but also for H⁺ with the “implicit” physical/chemical nonequilibrium, as the “explicit” physical/chemical nonequilibrium decouples the kinetics for pH and silicate. The failure to capture pH variation underestimated the mass transfer rate constant of protons when using the “implicit” physical/chemical nonequilibrium. This also suggested that variations in pH could be a proxy for investigating the rate of processes governed by the physical nonequilibrium. For NA, the overall breakthrough behavior of NA and pH was well described when ω_{overall} is set to 2.35 h⁻¹, yet the pH time evolution showed no proton release during the transport experiment (Figure S9b). Parameters used in the “implicit” approach were summarized in Table S4.

Overall, this implicit model approach could be used as a simplified method to describe the mobility of reactive compounds, although variations in pH could not be systematically predicted. This can be a benefit when reaction rate constants are difficult

to acquire, and the internal pores of mineral assemblages host a significant proportion of reactive surface sites.

3.2. Effect of diffusion-controlled mass transfer on synergistic or competitive binding

As reported in previous work,⁴¹ NA and NFA exerted a mutual effect on their breakthrough behavior under flow. Indeed, the experimental BTC for NFA exhibited a two-step behavior in GCS column, whereas the BTC for NA tailed extensively before reaching a total breakthrough (Figure 3a). This behavior was explained to result from NA-NFA dimer formation on goethite, and stabilized by hydrogen bonding and van der Waals interactions.^{17,22} These interactions effectively enhanced the NFA binding, which is otherwise low. We applied the previously published approach⁴¹ by combining co-binding reactions and NA adsorption kinetics without modifying the forward and backward kinetic rate constants of NA. Here, occurrence of co-binding reactions was assumed to be instantaneous at the molecular reaction scale and the apparent reaction rates were assumed to be limited by adsorption kinetics of NA. The modeled BTCs captured the mobility behavior of both NFA and NA (Figure 3a).

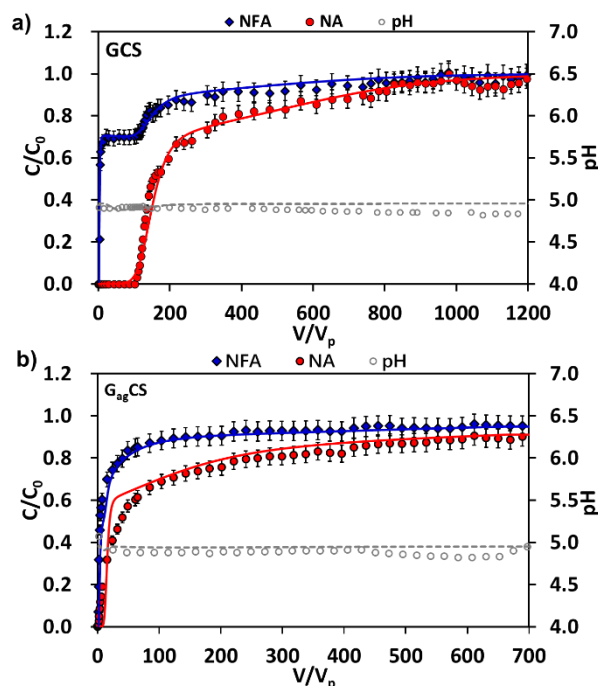


Figure 3. Experimental and modeled BTCs for NA and NFA in GCS (a) and $G_{ag}CS$ columns (b).

Inflow conditions: $[NA] = 10 \mu M$, $[NFA] = 10 \mu M$, flow rate = 0.5 mL/min, 10-mM NaCl background electrolyte, inflow pH 5.0 ± 0.1 . Pore volumes of GCS columns and $G_{ag}CS$ columns are 4.3 ± 0.1 mL and 4.1 ± 0.1 mL, respectively. Solid lines and dashed lines are modeled BTCs obtained using

PHREEQC-2. Points represent the experimental data points.

Surprisingly, in the $G_{ag}CS$ system the experimental BTCs for NFA adopted a classical sigmoidal shape (i.e., one step behavior akin to that of NA) and both compounds underwent faster breakthrough and extended long tailing. After ~ 550 PV, the experimental BTCs for NA and NFA reached a plateau at relative concentrations of ~ 0.9 and ~ 0.95 , respectively. This finding suggests that the NFA breakthrough behaviors of NA are the result of by co-binding. Here, the physical non-equilibrium led

to slower NA adsorption onto goethite and therefore limited the occurrence of co-binding reactions. This finding may also explain why the observed two-step behavior of NFA in GCS column disappeared in the $G_{ag}CS$ column.

Attempts were made to simulate the transport of NA and NFA in $G_{ag}CS$ column via both explicit model (Fig. S10) and implicit model (Fig. 3b) approaches. The occurrence of co-binding reactions was assumed to be instantaneous, and thus was rate-limited by NA adsorption kinetics. An overall mass transfer coefficient $\omega_{overall}$ of 1.44 h^{-1} was also used to describe the apparent sorption dynamic of NA and NFA. For both modeling approaches we found that the modeled BTCs were relatively in good agreement with experimental BTCs (Figure S10 and Figure 3b). With the assistance of these modeling results, we suggest that coupled processes of physical and chemical nonequilibria may explain the concomitancy of earlier breakthrough and very long tailing. This would consequently explain the discrepancy in the transport behavior of NFA and NA in GCS vs. $G_{ag}CS$ systems. The modeling results also support the occurrence of NA/NFA co-binding reactions in $G_{ag}CS$ columns.

We also compared the co-transport of NA and P in GCS and $G_{ag}CS$ columns (Figure 4). In the GCS column, the experimental BTC for P exhibited a sigmoidal-like shape, whereas the experimental BTC for NA was characterized by a prominent desorption front in the range of $\sim 25\text{--}65\text{ PV}$ after a short adsorption front and before reaching a plateau at $C/C_0 = 1$ (Figure 4a). A significant extent of NA desorption was observed for P adsorption, as NA surface loadings in the GCS column decreased from the maximum

at $\sim 0.05 \text{ NA/nm}^2$ at the middle of the breakthrough experiment to $\sim 0.03 \text{ NA/nm}^2$ at the end of the breakthrough experiment.

In $G_{\text{ag}}\text{CS}$ column, the experimental BTC of P was characterized by a regular asymmetrical shape, whereas that of NA exhibited faster breakthrough (Figure 4b). Unlike the GCS column, there was no significant desorption front of NA in $G_{\text{ag}}\text{CS}$ column, but similar total surface loadings were observed for P ($\sim 1.10 \text{ P/nm}^2$) and NA ($\sim 0.02 \text{ NA/nm}^2$) in both columns.

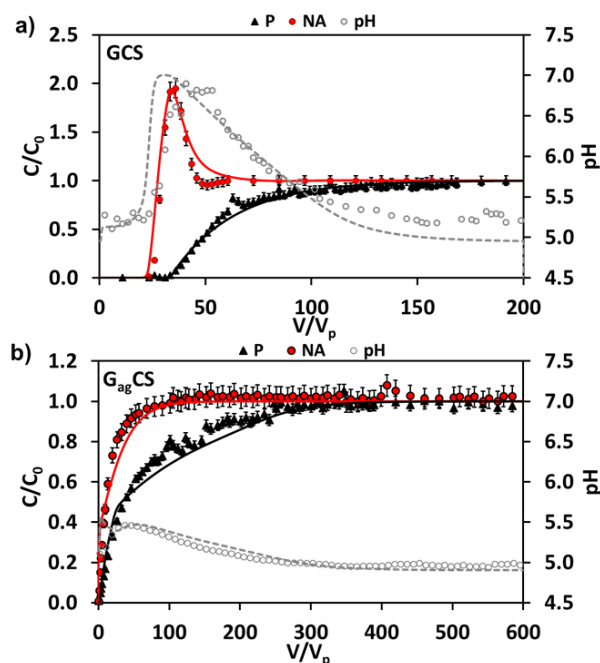


Figure 4. Experimental and modeled BTCs for NA and P in GCS (a) and $G_{\text{ag}}\text{CS}$ columns (b). Inflow conditions: $[\text{NA}] = 10 \mu\text{M}$, $[\text{P}] = 100 \mu\text{M}$, flow rate = 0.5 mL/min , 10-mM NaCl background electrolyte, inflow pH 5.0 ± 0.1 . Pore volumes of GCS columns and $G_{\text{ag}}\text{CS}$ columns are $4.3 \pm 0.1 \text{ mL}$ and $4.1 \pm 0.1 \text{ mL}$, respectively. Solid lines and dashed lines are modeled BTCs obtained using PHREEQC-2. The points represent the experimental data points.

442

443 To describe the co-mobility of NA and P in GCS column, surface complexation
444 reactions of NA and P (considering both monodentate and bidentate complexes), two-
445 step kinetic surface reaction expression of NA, and a single-rate surface reaction
446 expression of P were combined with ADE transport module. The calculated BTCs for
447 NA, P, and pH fitted the experimental results (Figure 4a) with a kinetic rate constant of
448 P sorption of 0.24 h^{-1} , and using all previously obtained parameters for NA (Table S1
449 and S3).

450 In the $G_{\text{ag}}\text{CS}$ column, surface complexation parameters of P were integrated into the
451 previously developed MIM transport model for NA without modifying the forward and
452 backward kinetic rate constants of NA as well as the mass transfer coefficient ω . As
453 shown in Figure S11, the calculations describe the BTCs for P and pH, but not for NA.
454 Another possibility to improve the modeling is to consider first the P adsorption—i.e.,
455 most surface hydroxo groups of goethite are likely first occupied by P before injection
456 of NA and P. This assumption, motivated by the greater affinity of P to goethite,⁴² has
457 allowed for a better fitting of the BTC for NA as shown in Figure 4b.

458 Collectively, these results show that a diffusion-controlled process within particle
459 aggregates alters cooperative or competitive binding and the mobility of reactive solutes.
460 As the co-interactions at the surface generally depend on the local concentration of each
461 species, decreasing the solute mass transported into the intra-aggregate zones per time
462 unit may change the surface speciation. In other words, the immobile water located at

intra-aggregate zones can act as a buffer zone, and this can slow down the mass transfer of solutes to reactive sorption sites located within the intra-aggregate zones.

3.3. Implications for the diffusion-controlled transport of environmental compounds in nature

Reactive mineral nanoparticle aggregation alters the mobility of the reactive solutes, yet it still allows a homogeneous flow. Aggregation favors the early breakthrough of NA and Si and extensive tailing in columns. This can be explained by a combination of physical and chemical non-equilibria. The solutes are subjected to physical non-equilibrium, restricting access to the immobile water fraction where the majority of sorption sites is present. As such, only a small number of reactive sites are in contact with the mobile water fraction. Under this condition, some solutes remain only in the mobile water fraction and may quickly go through the column. Other solutes diffuse from the mobile to the immobile water fraction, gaining access to more sorption sites. This may explain the concomitancy of the earlier breakthrough and the very long tailing, a phenomenon more pronounced in strongly sorbing solutes.

Small amounts of immobile water (~ 10% of the total porosity) did not drastically impact tracer transport, yet they had a great impact on reactive solute transport, especially when a significant portion of the sorption sites was located in the immobile water fraction (intra-aggregate zones). In these zones, diffusion from the mobile to the immobile water fractions, coupled with surface reactions, governed overall reaction

rates. We therefore conclude that sorption site localization and related local hydraulic conditions at pore-scale are the prevailing factors controlling contaminant transport, even under conditions of homogenous flow. To this, we add that water fractionation can also change competitive (desorption peaks above $C/C_0 = 1$) or synergistic (two-plateaus curves) shapes for BTCs into regular S-shaped BTCs.

This study also raised the importance of a consistent use of tracers for characterizing flow patterns and predicting reactive solute transfer. Nonreactive tracers reveal the main pattern of flow at the column scale but lack information on the local hydrodynamic conditions in the vicinity of sorption sites. Consequently, the injection of nonreactive tracers at the column scale may not be necessarily appropriate for characterizing local hydrodynamic conditions at the interface scale. Conversely, the use of reactive solutes, with a well-known chemistry and reactivity, could help probe changes in local hydrodynamic conditions. As such, by revealing difference in non-reactive and reactive solute transport through aggregated nanominerals, we expect that our work will help improve accurate characterization of flow within porous media, and even pave the way for designing better engineered reactive tracers.

Supporting Information

Synthesis of goethite, goethite aggregates and coatings materials; Control tests with the bare sand and reactivity and stability assessments with uncoated and coated sands; ATR-FTIR investigations and surface complexation modeling; Surface complexation modeling combined with kinetics and modeling parameters; Analysis and modeling of

tracer breakthrough curves (BTCs), pulse and step injection, with and without stop flow;
Reactive transport modeling (PHREEQC2); Sensitivity analysis of mass transfer
coefficient ω and fraction of sorption sites in contact with mobile water, f ; Experimental
and modeled BTCs for NA, Si and P in GCS and G_{ag}CS columns.

Acknowledgements

The authors gratefully acknowledge the support of the Institut Universitaire de France,
the Swedish Research Council (2020-04853), the ANR (ANR INFLOW-21-CE29-
0008-01), and the CNRS (IEA 2018-2020).

References:

- (1) Bronick, C. J.; Lal, R. Soil Structure and Management: A Review. *Geoderma* **2005**, *124* (1), 3–22. <https://doi.org/10.1016/j.geoderma.2004.03.005>.
- (2) Guhra, T.; Ritschel, T.; Totsche, K. U. Formation of Mineral–Mineral and Organo–Mineral Composite Building Units from Microaggregate-Forming Materials Including Microbially Produced Extracellular Polymeric Substances. *Eur. J. Soil Sci.* **2019**, *70* (3), 604–615. <https://doi.org/10.1111/ejss.12774>.
- (3) Totsche, K. U.; Amelung, W.; Gerzabek, M. H.; Guggenberger, G.; Klumpp, E.; Knief, C.; Lehdorff, E.; Mikutta, R.; Peth, S.; Prechtel, A.; Ray, N.; Kögel-Knabner, I. Microaggregates in Soils. *J. Plant Nutr. Soil Sci.* **2018**, *181* (1), 104–136. <https://doi.org/10.1002/jpln.201600451>.
- (4) Durner, W. Hydraulic Conductivity Estimation for Soils with Heterogeneous Pore Structure. *Water Resour. Res.* **1994**, *30* (2), 211–223. <https://doi.org/10.1029/93WR02676>.
- (5) Brusseau, M. L.; Rao, P. S. C. Modeling Solute Transport in Structured Soils: A Review. *Geoderma* **1990**, *46* (1), 169–192. [https://doi.org/10.1016/0016-7061\(90\)90014-Z](https://doi.org/10.1016/0016-7061(90)90014-Z).
- (6) van Genuchten, M. T.; Wierenga, P. J. Mass Transfer Studies in Sorbing Porous Media I. Analytical Solutions 1. *Soil Sci. Soc. Am. J.* **1976**, *40* (4), 473–480. <https://doi.org/10.2136/sssaj1976.03615995004000040011x>.
- (7) Nkedi-Kizza, P.; Biggar, J. W.; Selim, H. M.; Van Genuchten, M. T.; Wierenga, P. J.; Davidson, J. M.; Nielsen, D. R. On the Equivalence of Two Conceptual Models for Describing Ion Exchange during Transport through an Aggregated Oxisol. *Water Resour. Res.* **1984**, *20* (8), 1123–1130.

- 538 (8) Sardin, M.; Schweich, D.; Leij, F.; Genuchten, M. T. Modeling the Nonequilibrium Transport of
539 Linearly Interacting Solutes in Porous Media: A Review. *Water Resour. Res.* **1991**, 27 (9), 2287–
540 2307.
- 541 (9) Stumm, W.; Sigg, L.; Sulzberger, B. *Chemistry of the Solid-Water Interface: Processes at the*
542 *Mineral-Water and Particle-Water Interface in Natural Systems*; Wiley: New York, 1992.
- 543 (10) Cornell, R. M.; Schwertmann, U. *The Iron Oxides: Structure, Properties, Reactions,*
544 *Occurrences and Uses*; John Wiley & Sons, 2003.
- 545 (11) Stumm, W.; Sulzberger, B. The Cycling of Iron in Natural Environments: Considerations Based
546 on Laboratory Studies of Heterogeneous Redox Processes. *Geochim. Cosmochim. Acta* **1992**, 56
547 (8), 3233–3257. [https://doi.org/10.1016/0016-7037\(92\)90301-X](https://doi.org/10.1016/0016-7037(92)90301-X).
- 548 (12) Hanna, K.; Carteret, C. Sorption of 1-Hydroxy-2-Naphthoic Acid to Goethite, Lepidocrocite and
549 Ferrihydrite: Batch Experiments and Infrared Study. *Chemosphere* **2007**, 70 (2), 178–186.
550 <https://doi.org/10.1016/j.chemosphere.2007.06.035>.
- 551 (13) Polya, D.; Charlet, L. Rising Arsenic Risk? *Nat. Geosci.* **2009**, 2 (6), 383–384.
552 <https://doi.org/10.1038/ngeo537>.
- 553 (14) Hanna, K.; Boily, J.-F. Sorption of Two Naphthoic Acids to Goethite Surface under Flow through
554 Conditions. *Environ. Sci. Technol.* **2010**, 44 (23), 8863–8869. <https://doi.org/10.1021/es102903n>.
- 555 (15) Ona-Nguema, G.; Morin, G.; Juillot, F.; Calas, G.; Brown, G. E. EXAFS Analysis of Arsenite
556 Adsorption onto Two-Line Ferrihydrite, Hematite, Goethite, and Lepidocrocite. *Environ. Sci.*
557 *Technol.* **2005**, 39 (23), 9147–9155. <https://doi.org/10.1021/es050889p>.
- 558 (16) Karpov, M.; Seiwert, B.; Mordehay, V.; Reemtsma, T.; Polubesova, T.; Chefetz, B.
559 Transformation of Oxytetracycline by Redox-Active Fe(III)- and Mn(IV)-Containing Minerals:

Processes and Mechanisms. *Water Res.* **2018**, *145*, 136–145.
<https://doi.org/10.1016/j.watres.2018.08.015>.

(17) Xu, J.; Marsac, R.; Costa, D.; Cheng, W.; Wu, F.; Boily, J.-F.; Hanna, K. Co-Binding of Pharmaceutical Compounds at Mineral Surfaces: Molecular Investigations of Dimer Formation at Goethite/Water Interfaces. *Environ. Sci. Technol.* **2017**, *51* (15), 8343–8349.
<https://doi.org/10.1021/acs.est.7b02835>.

(18) Hofmann, A.; Pelletier, M.; Michot, L.; Stradner, A.; Schurtenberger, P.; Kretzschmar, R. Characterization of the Pores in Hydrous Ferric Oxide Aggregates Formed by Freezing and Thawing. *J. Colloid Interface Sci.* **2004**, *271* (1), 163–173.
<https://doi.org/10.1016/j.jcis.2003.11.053>.

(19) Hem, J. D. *Study and Interpretation of the Chemical Characteristics of Natural Water*; Department of the Interior, US Geological Survey, 1985; Vol. 2254.

(20) Kümmerer, K. Antibiotics in the Aquatic Environment – A Review – Part I. *Chemosphere* **2009**, *75* (4), 417–434. <https://doi.org/10.1016/j.chemosphere.2008.11.086>.

(21) Zhang, T.; Li, B. Occurrence, Transformation, and Fate of Antibiotics in Municipal Wastewater Treatment Plants. *Crit. Rev. Environ. Sci. Technol.* **2011**, *41* (11), 951–998.
<https://doi.org/10.1080/10643380903392692>.

(22) Xu, J.; Marsac, R.; Wei, C.; Wu, F.; Boily, J.-F.; Hanna, K. Cobinding of Pharmaceutical Compounds at Mineral Surfaces: Mechanistic Modeling of Binding and Cobinding of Nalidixic Acid and Niflumic Acid at Goethite Surfaces. *Environ. Sci. Technol.* **2017**, *51* (20), 11617–11624.
<https://doi.org/10.1021/acs.est.7b02900>.

- 581 (23) Rahnemaie, R.; Hiemstra, T.; van Riemsdijk, W. H. Geometry, Charge Distribution, and Surface
582 Speciation of Phosphate on Goethite. *Langmuir* **2007**, *23* (7), 3680–3689.
583 <https://doi.org/10.1021/la062965n>.
- 584 (24) Hiemstra, T.; Barnett, M. O.; van Riemsdijk, W. H. Interaction of Silicic Acid with Goethite. *J.*
585 *Colloid Interface Sci.* **2007**, *310* (1), 8–17. <https://doi.org/10.1016/j.jcis.2007.01.065>.
- 586 (25) Kanematsu, M.; Waychunas, G. A.; Boily, J.-F. Silicate Binding and Precipitation on Iron
587 Oxyhydroxides. *Environ. Sci. Technol.* **2018**, *52* (4), 1827–1833.
588 <https://doi.org/10.1021/acs.est.7b04098>.
- 589 (26) Gaboriaud, F.; Ehrhardt, J.-J. Effects of Different Crystal Faces on the Surface Charge of
590 Colloidal Goethite (α -FeOOH) Particles: An Experimental and Modeling Study. *Geochim.*
591 *Cosmochim. Acta* **2003**, *67* (5), 967–983.
- 592 (27) Marsac, R.; Martin, S.; Boily, J.-F.; Hanna, K. Oxolinic Acid Binding at Goethite and Akaganéite
593 Surfaces: Experimental Study and Modeling. *Environ. Sci. Technol.* **2016**, *50* (2), 660–668.
594 <https://doi.org/10.1021/acs.est.5b04940>.
- 595 (28) Rusch, B.; Hanna, K.; Humbert, B. Coating of Quartz Silica with Iron Oxides: Characterization
596 and Surface Reactivity of Iron Coating Phases. *Colloids Surf. Physicochem. Eng. Asp.* **2010**, *353*
597 (2), 172–180. <https://doi.org/10.1016/j.colsurfa.2009.11.009>.
- 598 (29) Greenberg, A. E.; Clesceri, L. S.; Eaton, A. D. *Standard Methods for the Examination of Water*
599 *and Wastewater*; American Public Health Association, 1992.
- 600 (30) Parkhurst, D. L.; Appelo, C. A. J. User's Guide to PHREEQC (Version 2): A Computer Program
601 for Speciation, Batch-Reaction, One-Dimensional Transport, and Inverse Geochemical
602 Calculations. *Water-Resour. Investig. Rep.* **1999**, *99* (4259), 312.

- 603 (31) Hiemstra, T.; Van Riemsdijk, W. H. A Surface Structural Approach to Ion Adsorption: The
 604 Charge Distribution (CD) Model. *J. Colloid Interface Sci.* **1996**, *179* (2), 488–508.
 605 <https://doi.org/10.1006/jcis.1996.0242>.
- 606 (32) van Genuchten, M. Th.; Wagenet, R. J. Two-Site/Two-Region Models for Pesticide Transport
 607 and Degradation: Theoretical Development and Analytical Solutions. *Soil Sci. Soc. Am. J.* **1989**,
 608 *53* (5), 1303–1310. <https://doi.org/10.2136/sssaj1989.03615995005300050001x>.
- 609 (33) Liu, C.; Zachara, J. M.; Qafoku, N. P.; Wang, Z. Scale-Dependent Desorption of Uranium from
 610 Contaminated Subsurface Sediments. *Water Resour. Res.* **2008**, *44* (8).
 611 <https://doi.org/10.1029/2007WR006478>.
- 612 (34) Lassabatere, L.; Winiarski, T.; Galvez-Cloutier, R. Retention of Three Heavy Metals (Zn, Pb,
 613 and Cd) in a Calcareous Soil Controlled by the Modification of Flow with Geotextiles. *Environ.*
 614 *Sci. Technol.* **2004**, *38* (15), 4215–4221. <https://doi.org/10.1021/es035029s>.
- 615 (35) Lassabatere, L.; Spadini, L.; Delolme, C.; Février, L.; Galvez Cloutier, R.; Winiarski, T.
 616 Concomitant Zn-Cd and Pb Retention in a Carbonated Fluvio-Glacial Deposit under Both Static
 617 and Dynamic Conditions. *Chemosphere* **2007**, *69* (9), 1499–1508.
- 618 (36) Masciopinto, C.; Passarella, G. Mass-Transfer Impact on Solute Mobility in Porous Media: A
 619 New Mobile-Immobile Model. *J. Contam. Hydrol.* **2018**, *215*, 21–28.
 620 <https://doi.org/10.1016/j.jconhyd.2018.06.004>.
- 621 (37) Axe, K.; Persson, P. Time-Dependent Surface Speciation of Oxalate at the Water-Boehmite (γ -
 622 AlOOH) Interface: Implications for Dissolution. *Geochim. Cosmochim. Acta* **2001**, *65* (24),
 623 4481–4492. [https://doi.org/10.1016/S0016-7037\(01\)00750-5](https://doi.org/10.1016/S0016-7037(01)00750-5).

- 624 (38) Zhou, L.; Cheng, W.; Marsac, R.; Boily, J.-F.; Hanna, K. Silicate Surface Coverage Controls
625 Quinolone Transport in Saturated Porous Media. *J. Colloid Interface Sci.* **2022**, *607*, 347–356.
626 <https://doi.org/10.1016/j.jcis.2021.08.142>.
- 627 (39) Liu, C.; Shang, J.; Kerisit, S.; Zachara, J. M.; Zhu, W. Scale-Dependent Rates of Uranyl Surface
628 Complexation Reaction in Sediments. *Geochim. Cosmochim. Acta* **2013**, *105*, 326–341.
629 <https://doi.org/10.1016/j.gca.2012.12.003>.
- 630 (40) Badruzzaman, M.; Westerhoff, P.; Knappe, D. R. U. Intraparticle Diffusion and Adsorption of
631 Arsenate onto Granular Ferric Hydroxide (GFH). *Water Res.* **2004**, *38* (18), 4002–4012.
632 <https://doi.org/10.1016/j.watres.2004.07.007>.
- 633 (41) Luo, T.; Xu, J.; Cheng, W.; Zhou, L.; Marsac, R.; Wu, F.; Boily, J.-F.; Hanna, K. Interactions of
634 Anti-Inflammatory and Antibiotic Drugs at Mineral Surfaces Can Control Environmental Fate
635 and Transport. *Environ. Sci. Technol.* **2022**, *56* (4), 2378–2385.
636 <https://doi.org/10.1021/acs.est.1c06449>.
- 637 (42) Köhne, J. M.; Köhne, S.; Šimůnek, J. A Review of Model Applications for Structured Soils: A)
638 Water Flow and Tracer Transport. *J. Contam. Hydrol.* **2009**, *104* (1), 4–35.
639 <https://doi.org/10.1016/j.jconhyd.2008.10.002>.
- 640
- 641